The Responses of Antarctic sea ice and Overturning Cells to Meridional Wind Forcing

Hajoon Song[1,2], Yeonju Choi[1], Edward W. Doddridge[3], John Marshall[4]

[1]Department of Atmospheric Sciences, Yonsei University, Seoul, South Korea
[2]Division of Environmental Science & Engineering, Pohang University of Science and Technology, Pohang, Republic of Korea
[3]Australian Antarctic Program Partnership, Institute for Marine and Antarctic Studies, University of Tasmania, nipaluna / Hobart, Tasmania, Australia
[4]Department of Earth, Atmospheric and Planetary Sciences, Massachusetts Institute of Technology, Cambridge, Massachusetts, USA

Key Points:

- The southerly wind anomaly over the Antarctic seasonal ice zone enhances the seasonality of sea ice extent and volume.
- Southerly wind anomalies increase buoyancy loss at leads and polynyas, and strengthen the lower meridional overturning circulation cell.
- Northerly wind anomalies result in opposite responses in the seasonality of the sea ice volume, ocean states and lower cell.

Corresponding author: Hajoon Song, `hajsong@yonsei.ac.kr`

Abstract

Meridional winds over the seasonal ice zone (SIZ) of the Antarctic have undergone changes and likely contributed to sea ice extent variability in recent decades. In this study, using observations and an eddy-resolving channel model of the Antarctic SIZ, we investigate the influence of meridional wind changes on the sea ice distribution, and document how the underlying ocean might change. We find that southerly wind anomalies in austral winter lead to an increase in sea ice extent by encouraging equatorward sea ice drift. This results in more leads and polynyas, ice production and buoyancy loss near the coastal region and freshening out in the open ocean near the Antarctic Circumpolar Current. In contrast, southerly wind anomalies in austral summer reduce sea ice extent due to warming anomalies near the sea ice edge. This is a consequence of enhanced meridional overturning circulation (MOC) triggered by enhanced buoyancy loss through surface heat flux and brine rejection, which brings relatively warm water towards the summertime sea ice edge. A water-mass transformation analysis reveals the increased deep water formation caused by brine rejection and heat loss in leads and polynyas. Changes in sea ice extent and MOC behave in the opposite way when the sign of the wind anomaly is switched from southerly to northerly. Our study shows that meridional wind anomalies can modify not only the sea ice distribution, extent of polynyas and air-sea buoyancy fluxes, but also the ocean's MOC and bottom water properties.

Plain Language Summary

We investigate the changes in the seasonal ice zone of the Antarctic to meridional wind stress using observations and a numerical ocean model and find that the responses in summer and winter are opposites. Under stronger southerly winds, the wintertime sea ice edge extends further toward the equator, accompanying freshening of the Antarctic Circumpolar Current and more polynyas near the continental shelf. Active sea ice production occurs at those polynyas, resulting in brine rejection, deep convection and intensification of the lower cell. In summer, stronger southerly winds increase the surface temperature near the sea ice edge and cause the sea ice to retreat further towards the pole. With weaker southerly winds, the seasonal changes in the sea ice extent are reduced, leading to less sea ice production, weaker convection and the lower cell. This study highlights that the meridional wind, which has high uncertainty, has a substantial influence not only on the sea ice distribution and surface ocean state, but also on the meridional overturning of the Southern Ocean.

1 Introduction

The Antarctic sea ice is a crucial element in the complex interplay between the atmosphere and the ocean. While the sea ice typically impedes the exchange of heat and gases between the ocean and atmosphere, certain areas known as leads and polynyas allow for intense heat loss to occur (Campbell et al., 2019). This heat loss can trigger the formation of new sea ice and the subsequent salt flux into the ocean through brine rejection (Tamura et al., 2008a). These processes are critical for the ventilation of the ocean and the formation of deep water, highlighting the importance of Antarctic sea ice in the global climate system (Ferrari et al., 2014). Additionally, the regulation of heat and moisture fluxes by sea ice, along with its control on radiation, impacts atmospheric inversion (Pavelsky et al., 2011), low-level cloud formation (Wall et al., 2017), and tropospheric jet (Smith et al., 2017; Bader et al., 2013; Kidston et al., 2011) by modulating near-surface temperature and humidity. For example, the suppression of oceanic heat transfer due to sea ice strengthens atmospheric inversion, with its effect decreasing at higher altitudes (Pavelsky et al., 2011). These polar temperature changes affect baroclinic instability, altering the tropospheric jet's strength and location (Smith et al., 2017). Moreover, Antarctic sea ice plays a crucial role in the global climate system by influencing the carbon cycle (Stein et al., 2020).

Satellite observations show that the extent of Antarctic sea ice generally increased from the beginning of the record in the late 1970s until 2014, albeit with spatial and temporal variability (Cavalieri & Parkinson, 2008; Comiso & Nishio, 2008; Parkinson & Cavalieri, 2012). This increase in Antarctic sea ice contrasts the decrease in Arctic sea ice caused by global warming (Turner et al., 2009; Ferreira et al., 2015). This unintuitive increase in Antarctic sea ice has led to extensive related studies on its causes and mechanisms, such as changes in westerly winds (Purich et al., 2016; Thompson & Solomon, 2002), ocean currents and upwelling (Armour et al., 2016; Ferreira et al., 2015), freshwater input from ice sheets (Pauling et al., 2016; Bintanja et al., 2013; Rye et al., 2020), and meridional winds (Holland & Kwok, 2012; Haumann et al., 2014; Turner et al., 2016; Kwok et al., 2017)

In the Antarctic region, changes in sea ice extent are also associated with changes in the meridional wind (Holland & Kwok, 2012; Haumann et al., 2014; Turner et al., 2016; Kwok et al., 2017). Holland and Kwok (2012) show that changes in wind stress can account for the trend in sea ice drift and concentration in West Antarctica. Haumann et al. (2014) and Turner et al. (2016), using observations and atmospheric reanalysis, respectively, also suggest that changes in wind patterns associated with surface pressure systems are linked to changes in Antarctic sea ice on multidecadal time scales, although they differ in their explanation for these changes; Haumann et al. (2014) attribute it to anthropogenic stratospheric ozone depletion and greenhouse gas increase, while Turner et al. (2016) suggest it is due to intrinsic variability in the climate system. In addition, Kwok et al. (2017) attribute the trends in the meridional winds to the seasonal trends in the Antarctic sea ice extent.

The observed significant correlation between meridional wind anomalies and Antarctic sea ice trends is not fully understood due to the influences of multiple other factors. In particular, the zonal component of the wind over the Antarctic sea ice is generally stronger than the meridional component (Hazel & Stewart, 2019). The strong easterlies around Antarctica make it challenging to isolate the individual effects of meridional wind anomalies on regional sea ice trends. The southerly katabatic wind eventually contributes to the easterly as it is deflected to the left under the Coriolis force (Parish & Waight III, 1987). Furthermore, reliance on satellite observations can limit the detailed study of sea ice trends, especially during summer months. The large spread in the trends of meridional winds across various reanalysis products infers a high level of the uncertainty in estimating these changes (Bracegirdle & Marshall, 2012; Dong et al., 2020; Hobbs et al., 2020; Huai et al., 2019; Neme et al., 2022).

In this research, we employ an idealized 3-dimensional channel model with a 4 km horizontal resolution to investigate the responses of Antarctic sea ice and Southern Ocean circulation to changes in meridional wind intensity. Despite its simplifications, this idealized model captures the seasonal cycle of sea ice as well as key ocean circulation features, including the Antarctic Circumpolar Current, Antarctic Slope Current, and two-cell structure in the meridional overturning circulation (Doddridge et al., 2021). The aims of this study are to (1) examine the effects of meridional wind anomalies on sea ice concentration and its mechanisms during the summer and winter seasons, (2) explore how the changes in sea ice concentration affect water-mass transformation in the Southern

Ocean (3) investigate the impact on the ocean circulation, and (4) identify any potential feedback that may affect sea ice distribution. Our results show that meridional wind changes over the Antarctic sea ice trigger substantial changes in not only the sea ice concentration but also the ocean states and the strength of the lower cell, highlighting the complex interplay between these components and importance of lowering its uncertainty to more accurate simulation of the Southern Ocean circulation.

Our paper is organized as follows. In Section 2, we analyze the observations to identify the relationship between the meridional wind and Antarctic sea ice. We then describe our model, experimental design, and analysis methods in Section 3. The responses of the sea ice and ocean states to the meridional wind anomalies are presented in Section 4, while Section 5 presents the changes in ocean circulation and the associated water mass transformation rate. Finally, we summarize this study and discuss its implications in Section 6.

2 Observational analysis of meridional winds and sea ice extent

We analyze the relationship between meridional wind and Antarctic sea ice, focusing on sea ice concentration and 10-meter wind trends in March (minimum sea ice extent) and September (maximum extent) from 1980 to 2020 (Fig. 1). We obtained the monthly mean sea ice concentration data from the NASA National Snow and Ice Data Center (DiGirolamo et al., 2022), and the 10-meter wind data from the ERA5 Reanalysis (Hersbach et al., 2023).

In summer, there is a cyclonic trend over the Amundsen Sea, associated with the deepening of the Amundsen Sea Low (ASL), while anticyclonic trends over the Weddell Sea and Indian Ocean (Fig. 1(a)). The strengthening of both cyclone and anticyclone within the western Antarctic ocean accompanies strong northerly wind trends over the Antarctic Peninsula and southerly wind trends over the Ross Sea and the eastern Weddell Sea. Meanwhile, in winter during this period, only the strengthening tendency of ASL is significant with its center shifted southwestward (Fig. 1(b)). The contrast in sea ice concentration trends between the western and eastern regions of the Antarctic Peninsula may be related to changes in the ASL and associated meridional wind variability.

Scatter plots in Fig. 1(c,d) illustrate the relationship between anomalies of meridional wind and sea ice extent computed by summing areas weighted by their sea ice con-

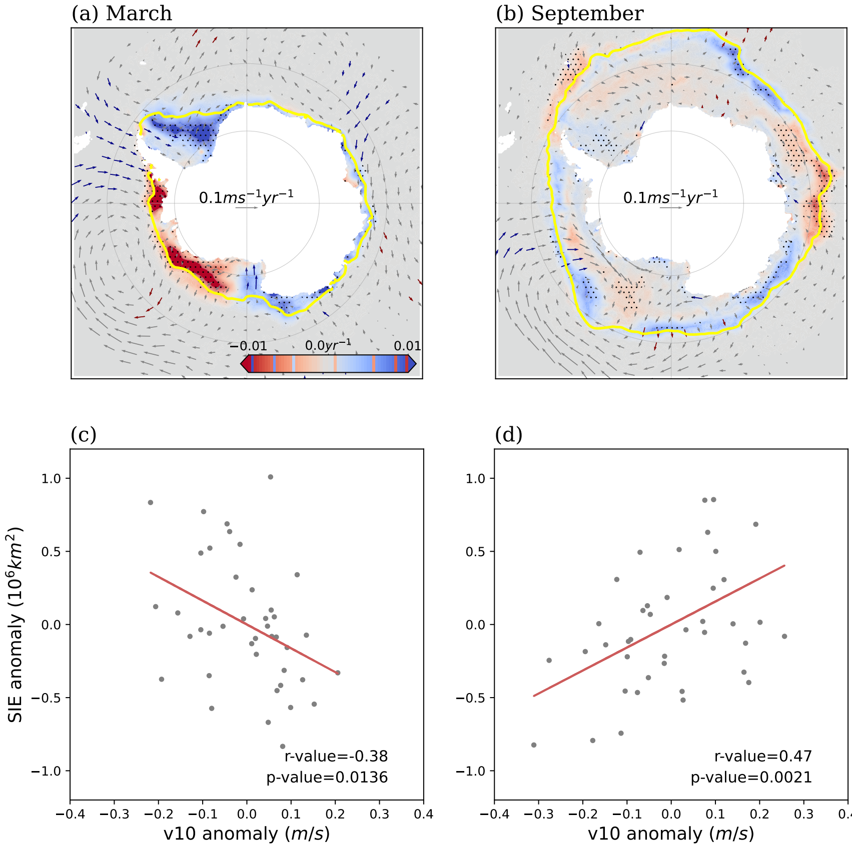

Figure 1. (a,b) The trend of sea ice concentration (SIC) (shades) and 10-meter wind (arrows) and (c,d) the relationships between the anomalies of sea ice extent and 10 m meridional wind for (a,c) March and (b,d) September during 1980-2020. In (a,b), stippling indicates SIC trends with >95% significance, while red and blue vectors signify positive and negative equatorward meridional wind (v10) trends with >90% significance. Yellow lines in (a,b) denote the average sea ice edge determined by the location where sea ice concentration is at 15%. Data sources: NSIDC satellite product (SIC) and ERA5 reanalysis data (10-meter wind).

centration greater than 15%. The positive correlation between them during the austral winter suggests that the anomalously strong southerly wind tends to extend the sea ice edge equatorward in winter (Fig. 1(d)). This positive correlation is consistent with the results of several previous studies (Holland & Kwok, 2012; Turner et al., 2016; Wagner et al., 2021; Stammerjohn et al., 2003; Harangozo, 2006). Austral summer, on the other hand, shows a negative relationship between meridional wind anomaly and sea ice extent anomaly, although this correlation is weaker (Fig. 1(c)). This weak correlation suggests that thermodynamic processes, driven by local radiative equilibrium or thermal advection within both the ocean and atmosphere, may play a bigger role in sea ice variability during summer months than dynamic redistribution by wind stress. Alternatively, it is difficult to dismiss the possibility that the strong winter correlation could influence summer sea ice minimum. Historically, there has been little relationship between the winter states and subsequent summer minimum (Libera et al., 2022), it may differ on larger time scales or due to rapid shifts in the Antarctic sea ice system.

Furthermore, uncertainties in the satellite sea ice data increase during summer months, as distinguishing melt ponds from open water and capturing rapid melting events become challenging. These results suggest the necessity for further analyses of how sea ice responds differently to meridional wind anomalies in summer and winter, and how these changes are related to ocean circulation. It is essential to investigate the underlying mechanisms that drive these observed correlations using a numerical model.

3 Experiments with an eddying channel model of the seasonal ice zone

3.1 Channel model

A channel model is prepared using MIT General Circulation Model (MITgcm) (Marshall, Hill, et al., 1997; Marshall, Adcroft, et al., 1997; Adcroft et al., 1997; Marshall et al., 1998; Adcroft et al., 2004) to represent the sea ice and ocean circulation in the Southern Ocean. The domain has a size of 1200 km by 3200 km in zonal and meridional directions, respectively, with 4 km resolution. There are 50 vertical levels from the surface to 4000 m. The upper 50 m is resolved at every 10 m, and the intervals between levels increases to 100 m toward the bottom. There is a 300 m deep, 80 km wide shelf near the southern boundary that drops to the bottom within 300 km (Fig. 2). The model has connected

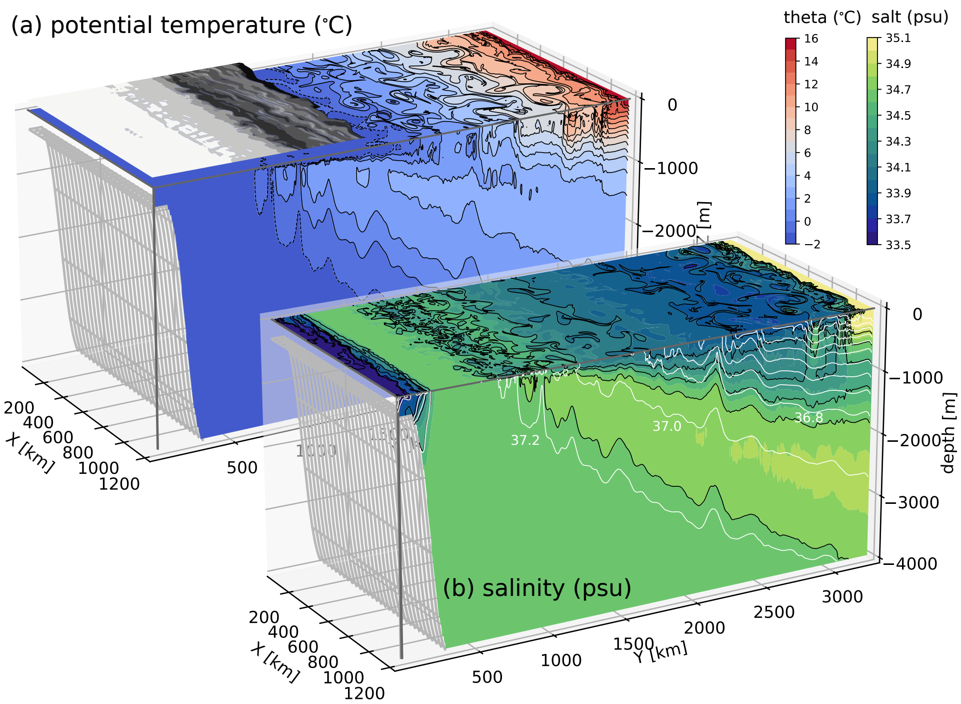

Figure 2. The channel with instantaneous (a) potential temperature (shading and black contours) along with sea ice fraction overlaid and (b) salinity (shading and black contours) and σ_2 (white contours), in austral winter (September 1^{st}). σ_2 contour interval is 0.2 kg m^{-3}.

east and west boundaries, allowing the flow to leave from one end and re-enter from the other, while the northern and southern boundaries are closed.

The temperature and salinity data from the World Ocean Atlas version 2 (Locarnini et al., 2013; Zweng et al., 2013) along 30°E were used to initialize the model domain. The data were extended zonally to cover the entire domain. The northern boundary has an approximately 100 km wide sponge layer where temperature and salinity are restored to the climatology with a timescale that changes from infinity at the southern edge to 10 days at the northern edge of the sponge. In addition, we simulate the dynamics and thermodynamics of sea ice by initializing the sea ice model with a 1 m thick ice cover south of 56°S.

The ocean in the channel was forced by the monthly mean atmospheric data from the Corrected Normal Year Forcing Version 2.0 product (Large & Yeager, 2009) through bulk formulae (Large & Pond, 1982). Similar to the initial condition, the values along

30°E were extended to cover the channel, so there is no variation in surface forcing in the zonal direction. The model was then integrated for 50 years with the vertical mixing computed by turbulent kinetic energy scheme by Gaspar et al. (1990) to reach quasi-equilibrium state.

3.2 Analysis in density coordinates

We evaluate the impact of meridional wind perturbations on the oceanic overturning circulation. The residual overturning circulation is the result of a balance between the wind-driven circulation and the circulation associated with eddies. In any given layer, the time-mean transport associated with the residual overturning circulation is written as

$$\overline{vh} = \overline{v}\overline{h} + \overline{v'h'}, \tag{1}$$

where h is the layer thickness, v is the meridional velocity in the layer, and the overbar and prime denote the time mean and the perturbation, respectively (Marshall & Speer, 2012; Pinardi et al., 2019). The transport weighted by the layer thickness is computed at every model time step using the LAYERS package in MITgcm (Abernathey et al., 2016), which allows the direct calculation of the residual overturning streamfunction. For this calculation, we define 122 classes of σ_2 (potential density referenced to 2000 dbar) covering from 33.5 to 37.8 kg m^{-3} with the varying interval of as little as 0.01 kg m^{-3} from 37.4 to 37.8 kg m^{-3}.

The residual overturning circulation can be further analyzed by examining the water-mass transformation rate. The changes in volume between isopycnal surfaces are primarily driven by the divergence of the advective volume flux along isopycnals and the volume flux across the isopycnal surfaces. The latter requires buoyancy fluxes, which change the density of water, and occurs either through surface buoyancy fluxes or diapycnal mixing across isopycnals. Our interest is on the contribution of surface buoyancy fluxes to the volume flux across isopycnal surfaces, which is also known as the water-mass transformation rate, and its relationship with the residual overturning circulation. This calculation is also done using the LAYERS package in MITgcm.

3.3 Meridional wind perturbation

We investigate the impact of meridional wind on the state of sea ice and the ocean, as well as water-mass transformation, by adding a perturbation to the meridional wind field south of 59°S. The wind perturbation, v'_{10m}, is defined as a function of latitude, ϕ, following,

$$v'_{10m}(\phi) = \frac{1}{\exp\left(-\left(\phi - \phi_0\right)/\lambda\right) + 1}. \tag{2}$$

With $\phi_0 = 62°S$ and $\lambda = 10/12°$, the size of wind perturbation becomes 0.5 at $\phi =$ 62°S and approaches 1 and 0 towards the pole and equator, respectively, within a few degrees of latitude (Fig. 3). This perturbation is applied to the monthly averaged meridional wind for the entire year. We refer to the simulation with this perturbation added to the meridional wind as $+v$, and to the simulation with this perturbation subtracted from the meridional wind as $-v$. The perturbation of 1 m s^{-1} is one order of magnitude smaller than the meridional wind correction used in previous studies (Kim & Stössel, 1998; Barthélemy et al., 2012), and is of similar magnitude to the standard deviation of the meridional wind (as shown in shading in Fig. 3). Moreover, the changes of the meridional wind over 10 years are in the order of 0.1 m s^{-1} yr^{-1} (Holland & Kwok, 2012), which all suggest that the size of perturbation used in this study is reasonable. With the initial condition taken from the 50-year of spin-up simulation, we integrate the channel model with this wind perturbation for 16 years and analyze the last 10 years by comparing the results with the control simulation (CTRL) where there is no meridional wind perturbation.

4 Response of sea ice and ocean states to meridional wind perturbations

4.1 Sea ice responses

The idealized channel model simulates the mean states of Antarctic sea ice and its seasonal variation with reasonable accuracy, despite its simple bathymetry and zonally symmetric surface forcing. Considering that the width of the channel model is roughly 7.5% of the circumference of the Antarctic Circle, the total sea ice extent in both summer and winter in CTRL are comparable with observations (not shown). Additionally, the annual sea ice production is approximately 900±22 km^3 when estimated using the sea ice fraction, the mean thickness and the area of each model grid. This is equivalent

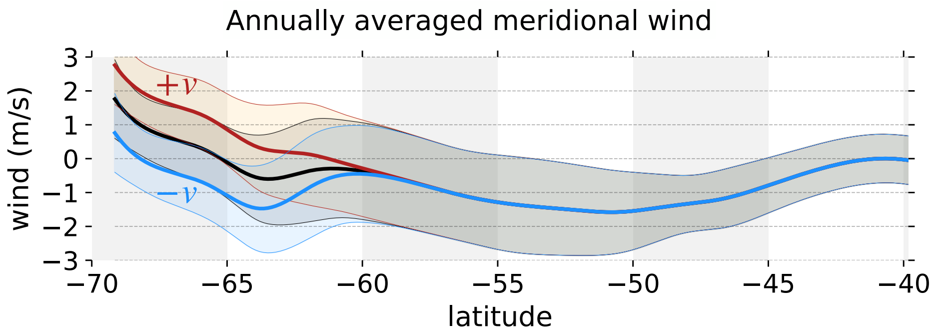

Figure 3. Zonally averaged meridional wind. The solid black, red and blue represent the annually averaged meridional wind in CTRL, $+v$ and $-v$, respectively, with the shading representing their standard deviation.

to approximately 13,950 km^3 if we linearly extend the production to the zonal length of the Southern Ocean, which is remarkably close to an observational estimate of 13,000 km^3 based on satellite observations (Tamura et al., 2008b).

The seasonality of sea ice extent is modified by the meridional wind perturbation. The $+v$ run produces a greater sea ice extent in winter but lower in summer compared to CTRL, whereas the $-v$ run shows the opposite pattern, with slightly lower sea ice extent in winter but greater in spring (Fig. 4(a)). Interestingly, changes in sea ice volume differ from those in sea ice extent (Fig. 4(b)). The $-v$ run shows the greatest sea ice volume throughout the year with the least seasonality. In $-v$, much of the sea ice is under the northerly wind (Fig. 3), which prevents the sea ice from drifting equatorward away from its formation site. As a result, the sea ice can grow more in $-v$ and becomes approximately 13% thicker than CTRL on average. In March, the sea ice thickness in $-v$ is nearly 30% greater than CTRL. On the other hand, the $+v$ run exhibits the largest seasonal variability of sea ice volume, indicating maximum sea ice production. In the final year of the simulation, sea ice production in $+v$ exceeded 1×10^3 km^3, nearly 70% greater than in $-v$. The greater seasonality in $+v$ suggests a more active equatorward freshwater transport by sea ice, leading to lower salinity with the melting of the sea ice following winter.

The impact of the meridional wind on the sea ice horizontal distribution is clearly evident from Fig. 4(c-e), which displays the sea ice concentration in July of the last sim-

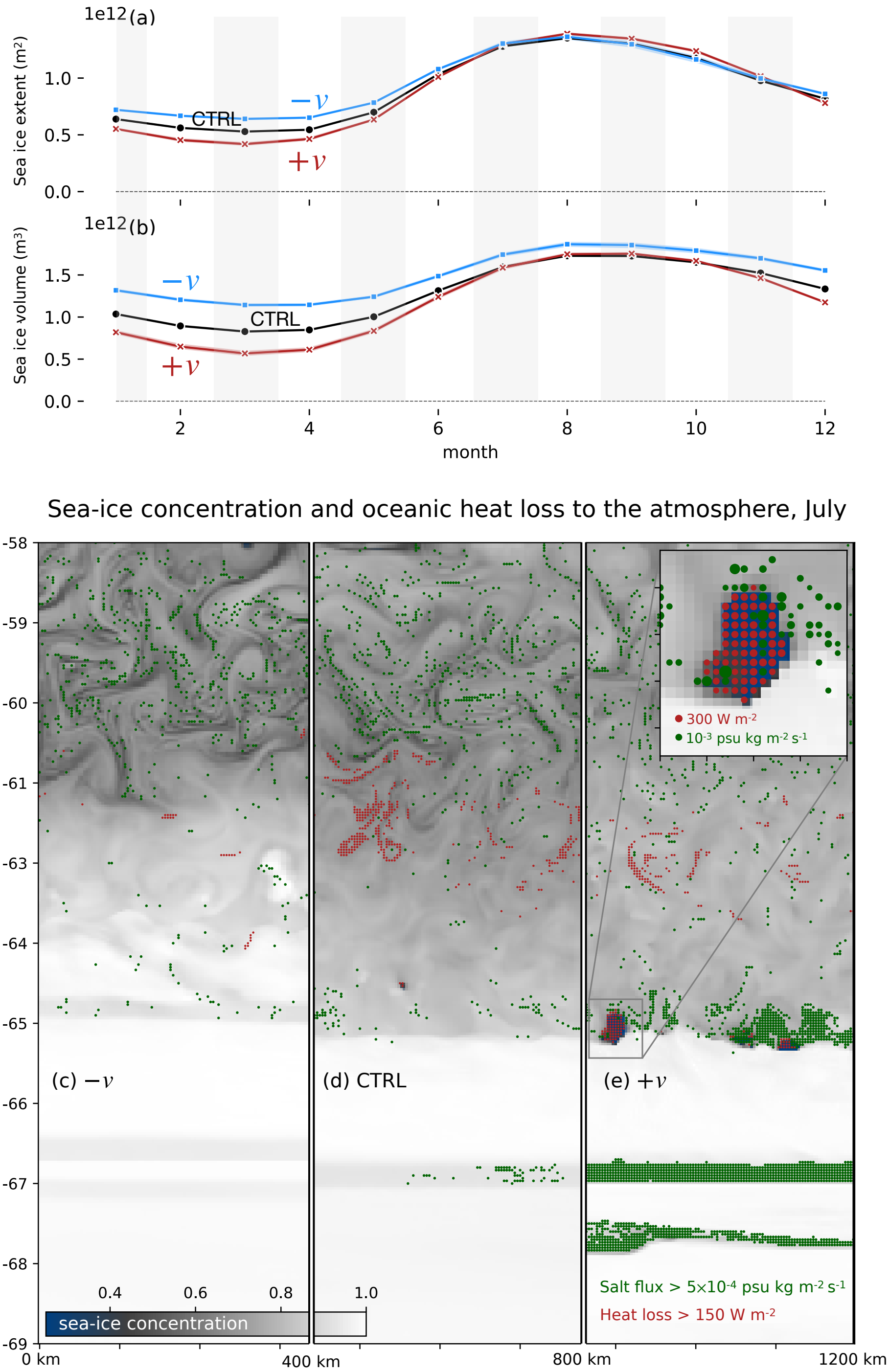

Figure 4. Solid lines are the monthly mean (a) sea ice extent and (b) sea ice volume from CTRL (black), $+v$ (red) and $-v$ (blue) over 10 years. The shadings, although not easily visible due to their small magnitude, indicate one standard deviation. The gray scale represents instantaneous sea ice concentration in (c) $-v$, (d) CTRL, and (e) $+v$ sampled in July. Red and green dots in (c-e) represents the grid points with the oceanic heat loss to the atmosphere greater than 150 W m-2 and the salt flux greater than 5×10^{-4} psu kg m^{-2} s^{-1}, respectively. The size of the red and green dots in the inset in (e) are scaled with reference to 300 W m-2 and 1×10^{-3} psu kg m^{-2} s^{-1}, respectively.

ulation year when the sea ice extends at least 58°S in all simulations. The visual comparison shows that the $-v$ run has the highest concentration between 65°S and 61°S, but the lowest concentration to the north of 61°S (Fig. 4(c)). In contrast, the $+v$ run exhibits the greatest sea ice concentration to the north of 61°S, but lower than the $-v$ run between 65°S and 61°S (Fig. 4(e)). In addition, there are polynyas near 65°S in $+v$ where the ocean loses massive quantities of heat (nearly 300 W m^{-2}) to the atmosphere (indicated by red dots in Fig. 4(e)). These polynyas, resulting from the divergence of sea ice driven by southerly wind, are also the site of sea ice production, leading to the density increase through brine rejection.

To the south of 65°S, $+v$ has the areas with the salt flux greater than 5×10^{-4} psu kg m^{-2} s^{-1} (green dots in Fig. 4(e)). These regions are largely ice covered (sea ice concentrations of greater than 80%), but have lower sea ice concentration than their surroundings with values close to 1 indicating complete sea ice coverage of the grid cell that may be associated with leads. Despite the sea ice concentration being greater than 0.8 in these areas, there is a continuous release of salt to the ocean due to ongoing sea ice production. Near the southern boundary, the ocean is largely isothermal at the freezing temperature. Heat fluxes into the atmosphere are therefore unable to directly increase the density of the underlying ocean and instead contribute to the formation of sea ice. The brine rejection associated with sea ice production shows up as regions of large salt fluxes. The forthcoming water-mass formation analysis in section 5.2 will further emphasize the importance of these regions for the circulation of the Southern Ocean.

We now analyse the sea ice changes in $+v$ and $-v$ using the sea ice volume (Φ) flux and its budget. Equatorward sea ice export is significantly larger during the ice growth season (from March to September) than the melt season (from September to March) (Fig. 5(a,b)) The maximum sea ice export occurs at 65°S (Fig. 5(b)), mainly as a result of large sea ice volume. The sea ice's movement is suppressed in the areas with higher ice concentration and thickness, where internal ice stress is strong. Another peak in sea ice export is observed near 59 to 60°S, driven by strong westerly winds causing a significant northward (or equatorward) sea ice drift when sea ice expands to this westerly band in late autumn. During the melt season, sea ice export significantly decreases (Fig. 5(a)), with certain summer months even experiencing a poleward export, likely due to northerly winds.

The meridional wind perturbation significantly alters the amount of sea ice export. In the $+v$ run, equatorward export increases throughout the sea ice zone, exhibiting a substantial export even near the coast at 69°S where there is nearly negligible export in the CTRL and $-v$ runs. This difference is due to stronger southerly winds in the $+v$. In contrast, the southerly wind in the $-v$ run is close to zero and sometimes reverses to become a northerly wind which compresses sea ice towards the coast. The pronounced ice export from the coastal region in the $+v$ run implies an increased production of sea ice near the coast in the $+v$ run, as anticipated in Fig. 4.

The analysis of the sea ice volume budget, as illustrated in Fig. 5(c-h), underscores the role of meridional wind-induced changes in sea ice production and distribution. The equation governing the evolution of zonal averaged ice volume, Φ, is

$$\frac{\partial \Phi}{\partial t} = -\frac{\partial (v_{ice}\Phi)}{\partial y} + \Gamma_\Phi. \tag{3}$$

The right hand side depicts two major contributors to the ice volume change. The first term represents the meridional transport of sea-ice volume, where v_{ice} denotes the meridional ice drift velocity. The second term, Γ_Φ, represents the thermodynamic processes, like freezing and melting. This budget analysis shows the latitudes where wind changes lead to additional sea ice freezing or melting, and further illustrates the balance between thermodynamic sources and dynamic redistribution in both season and latitude.

During the melt season, the time derivative of sea ice concentration is primarily governed by the thermodynamic sink (melting, Fig 5(c,g)) rather than the dynamic term (convergence of sea ice volume flux, Fig. 5(e)). In the growth season, equatorward of 65°S, dynamic redistribution generally makes a larger contribution to the sea ice volume changes and determines the position of the sea ice edge. Freezing and divergence largely counterbalance each other to the south of 65°S (Fig. 5(d,f,h)), which suggests an active manufacturing and equatorward transport of the sea ice there. This is particularly evident at the peaks at $66-67$°S and 65°S, areas characterized by leads and polynyas (Fig. 4(d)). This is consistent with the balance between dynamic/thermodynamic tendencies found by Schroeter and Sandery (2022).

The meridional wind perturbations clearly alter sea ice production and distribution (Fig. 5(c-h)). In the $+v$ run, the rate of sea ice volume change is larger than other simulations in both the growth and melt seasons (Fig. 5 (c,d)). Furthermore, the larger tendency in the sea ice volume is applied to almost all latitudes, which suggests that the seasonality of the sea ice volume is the largest in $+v$, consistent with Fig. 4(b). During the growth season, there is substantial additional freezing in the $+v$ run to the south of 65°S (Fig. 5(h)). This additional sea ice production increase the salt flux into the ocean, strengthening deep convection and the lower cell. Conversely, during the melt season, additional melting in the $+v$ run across most regions leads to a greater decrease in the sea ice volume (Fig. 5(g)) with minimal influence of dynamic redistribution (Fig. 5 (e)). In particular, greater melting at lower latitudes increases the freshwater flux, reducing the ocean salinity. The sea ice volume budget in $-v$ exhibits the opposite changes (Fig. 5(c,e,g)), suggesting that the northerly wind anomaly reduces the seasonality of the sea ice volume and lowers the salt and freshwater flux into the ocean at higher and lower latitudes, respectively.

4.2 Tracer distributions

A southerly wind anomaly in $+v$ over the sea ice area leads to substantial changes in temperature and salinity, not only near the sea ice region but also in the broader Southern Ocean (Fig. 6(a,b)). In winter, a positive salinity anomaly appears near the coastal shelf, which can be attributed to the increased brine rejection from enhanced sea ice production within more widespread leads and polynyas. The increased mixed layer depth reflects deeper convection from the enhanced sea ice production and salt flux into the ocean (Fig. 6(b)). In $+v$, the upper ocean north of the seasonal sea ice zone tends to be cooler and fresher than in CTRL, associated with the increased equatorward transport of cold and fresh water as inferred by the greater sea ice volume seasonality. At the subsurface, however, the temperature becomes up to 1°C warmer. The subsurface warming signal is attributed to the enhanced upwelling of warm subsurface water driven by stronger upper and lower cells in $+v$, as shown in Fig. 7. The surface warming at 65°S in summer is consistent with the surface expression of this warming and additional surface warming caused by sea ice loss leading to an increase in the absorption of incoming solar radiation. In summer, when the upper cell extends further south, this warming signal reaches the summer sea ice edge, leading to sea ice retreat to the south.

A northerly wind anomaly in $-v$ leads to responses which are generally opposite to those under the southerly wind anomaly; a decrease of salinity near the continental shelf, an increase of temperature and salinity to the north of the seasonal sea ice zone, and a negative anomaly of subsurface temperature that reaches the surface near the sea

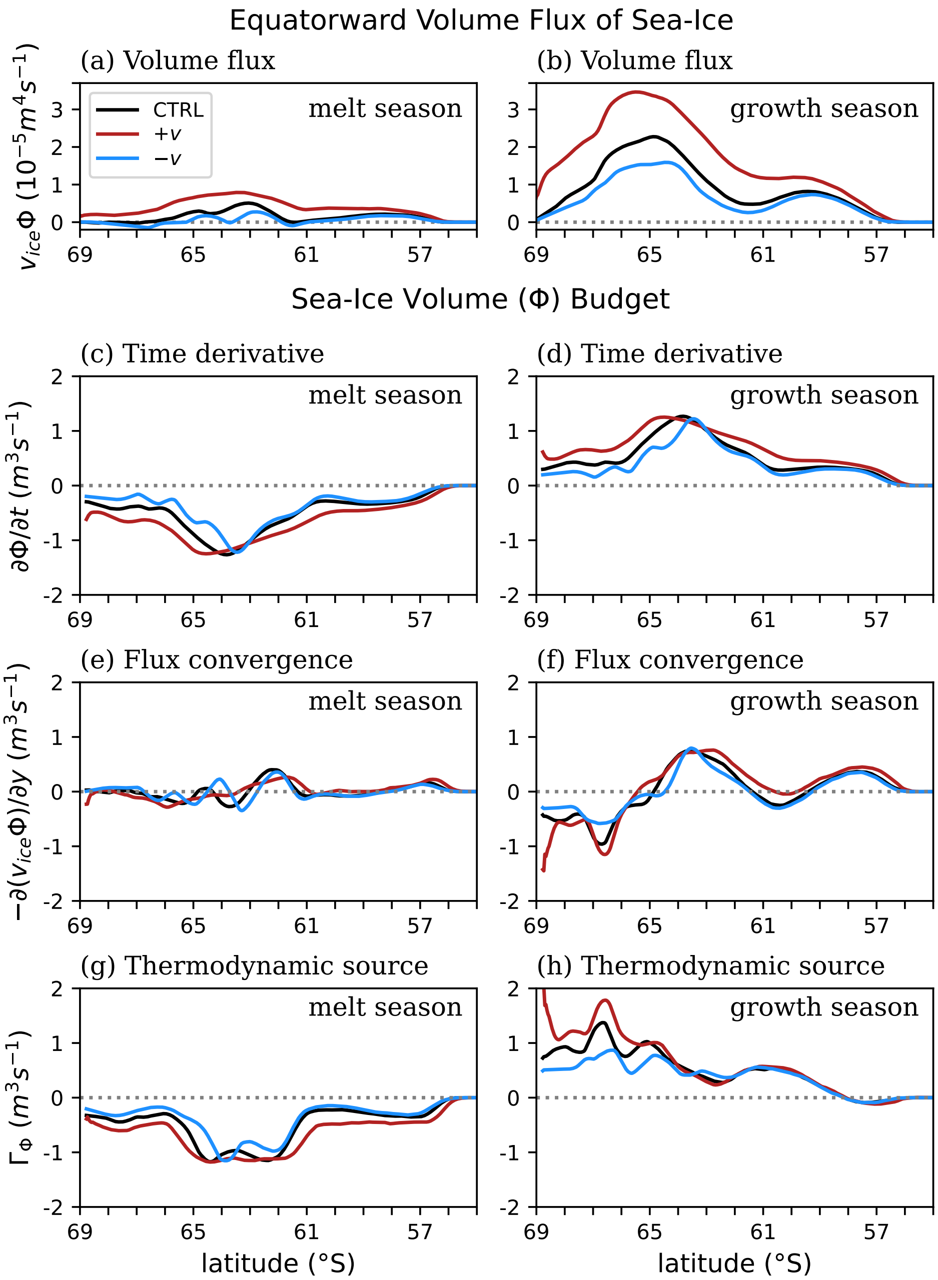

Figure 5. Equatorward flux of sea ice volume (Φ) (a-b) and the sea ice volume budgets (c-h) from CTRL, +v, -v simulations are shown. Left panels (a,c,e,g) correspond to the melt season (Sep-Mar), and right panels (b,d,f,h) to the growth season (Mar-Sep). The sea ice volume budgets include (c,d) time derivative ($\partial\Phi/\partial t$), (e,f) flux convergence ($-\partial(v_{ice}\Phi)/\partial y$), and (g,h) the thermodynamic source/sink (Γ_Φ).

ice edge in summer (Fig. 6(c,d)). The co-location of cooling and an increase in sea ice concentration at 65°S in the $-v$ simulation is consistent with enhanced ice coverage reducing the absorption of incoming solar radiation. The changes in surface conditions to the north of the seasonal sea ice zone are associated with a reduction in the equatorward transport of the cold and fresh water-mass, which is suggested by the smaller sea ice seasonality in the $-v$ run. The northerly wind anomaly increases the sea ice thickness, reduces the leads and polynyas, suppresses the salt flux into the ocean and convection in winter, as suggested by the shallower mixed layer depth (Fig. 6(d)). This reduction in the vertical mixing initiates the temperature anomaly in the seasonal sea ice zone, creating a dipole pattern (not shown). Then the absence of deep convection leads to the weakening of the lower cell with its center shifted equatorward, resulting in a subsurface cooling signal that reflects the changes in the lower cell (Fig. 7).

5 Changes in ocean circulation and the drivers

5.1 Overturning circulations

The channel model clearly represents the two overturning cells: the upper cell that transports the surface water equatorward and the lower cell that transports the surface water poleward (red and blue shading in Fig. 7, respectively). The streamfunction in σ_2 coordinates shows transport along density surfaces, except in the upper ocean where surface buoyancy fluxes change the density of the water (Fig. 7(a)). The upper and lower cell separate near the location of zero zonal wind stress where the divergence of water occurs due to the opposite direction of Ekman transport (not shown). The surface divergence is fed by an upwelling between two cells (Fig. 7(b)). The vertical upwelling velocity, w, is given by $\partial\Psi/\partial y$ where Ψ is the meridional streamfunction. The upwelling velocity can be up to $O(0.1)$ m day^{-1}. Deep convection occurs near 67°S and extends from the surface almost to the bottom of the domain. South of 67°S, the sea ice concentration is nearly 100% and there is rarely sea ice production in this channel model. In the control simulation (CTRL), the maximum size of the zonally-integrated, time-mean residual overturning streamfunction, Ψ, is -1.4 Sv.

The southerly wind anomaly in $+v$ has a significant impact on the residual overturning circulation, particularly the intensification of the lower cell (Fig. 7(b)). While the upper cell shows a slight increase in intensity, the intensification of the lower cell is

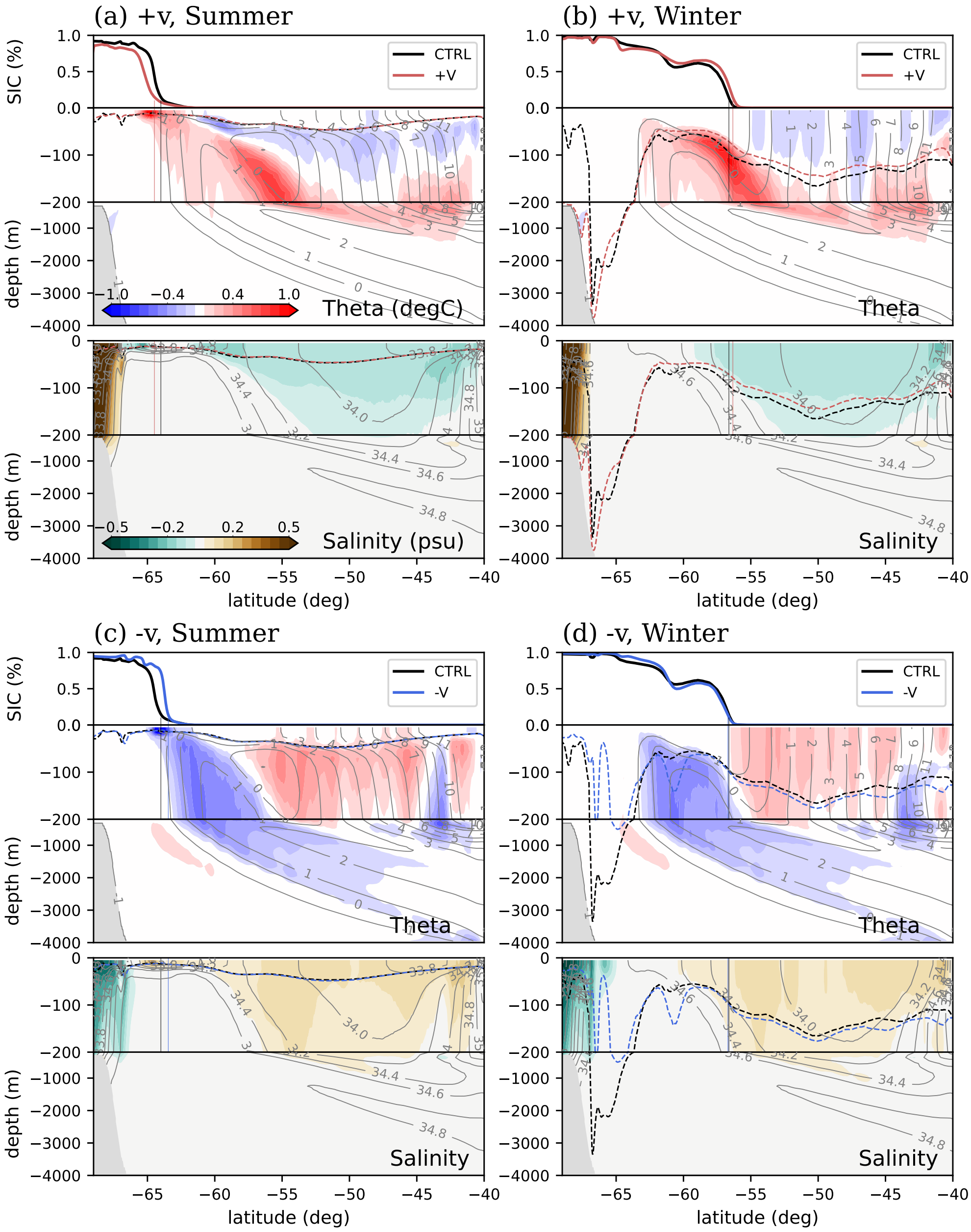

Figure 6. Temperature and salinity differences between the perturbed and control simulations are shown for austral summer (January-March) (a,c) and winter (July-September) (b,d). Grey contour lines depict the mean fields from control simulations. Dashed lines indicate the mixed layer depths in the control and perturbed simulations. The upper rectangle of each panel displays sea ice concentration as a function of latitude. Vertical lines represent the sea ice edges.

the dominant response to the southerly wind anomaly. This is evident in the time-mean Ψ, which has a maximum strength of -2.1 Sv, 50% stronger than that in CTRL. This intensification is driven by brine rejection where the sea ice concentration falls below 1 near 67°S (Fig. 4(e)). The strength of the upwelling branch between the upper and lower cells depends on the gradient of Ψ. Therefore the intensification of the lower cell leads to a stronger transport of warm subsurface water upwards towards the sea ice and potentially affects the sea ice.

In contrast, the northerly wind anomaly in $-v$ weakens the lower cell (Fig. 7(c)). The maximum strength of Ψ to the south of 60°S is less than -0.7 Sv, which is 50% weaker than that in CTRL. The reduced convection is related to the lower salt flux and heat loss in the region to the south of 65°S (Fig. 4(c)). The upper cell is also weaker under the northerly wind anomaly. As a result of the changes in the intensity of the upper and lower cells, the upwelling of relatively warm water becomes weaker than in CTRL, leading to the subsurface cooling.

5.2 Water-mass transformation rate

The impact of surface wind perturbations on deep convection implies that density changes are crucial in shaping ocean circulation. Therefore, understanding the relative contributions of heat and freshwater flux to these density changes is of great interest. In this section, we investigate the water-mass transformation rate to explore how meridional wind perturbations alter the surface buoyancy flux responsible for changes in the lower cell.

A volume of fluid of a uniform density will change when there is a flow, $\mathbf{v}$, through the isopycnals that confine this volume or when the interface of isopycnal moves with $\mathbf{v}_\sigma$ without actual volume flux. Then the diapycnal volume flux, $A(\sigma, t)$, can be expressed as

$$A(\sigma, t) = \iint_{\mathcal{A}_\sigma(\sigma,t)} (\mathbf{v} - \mathbf{v}_\sigma) \cdot \hat{\mathbf{n}}_\sigma d\mathcal{A}, \tag{4}$$

where $\mathcal{A}_\sigma(\sigma, t)$ is the area of isopycnal surface and $\hat{\mathbf{n}}_\sigma$ is a unit vector normal to the isopycnal surface pointing from low to high values. The diapycnal volume flux is further shown to be related to the non-advective supply of buoyancy (Walin, 1982; Marshall et al., 1999;

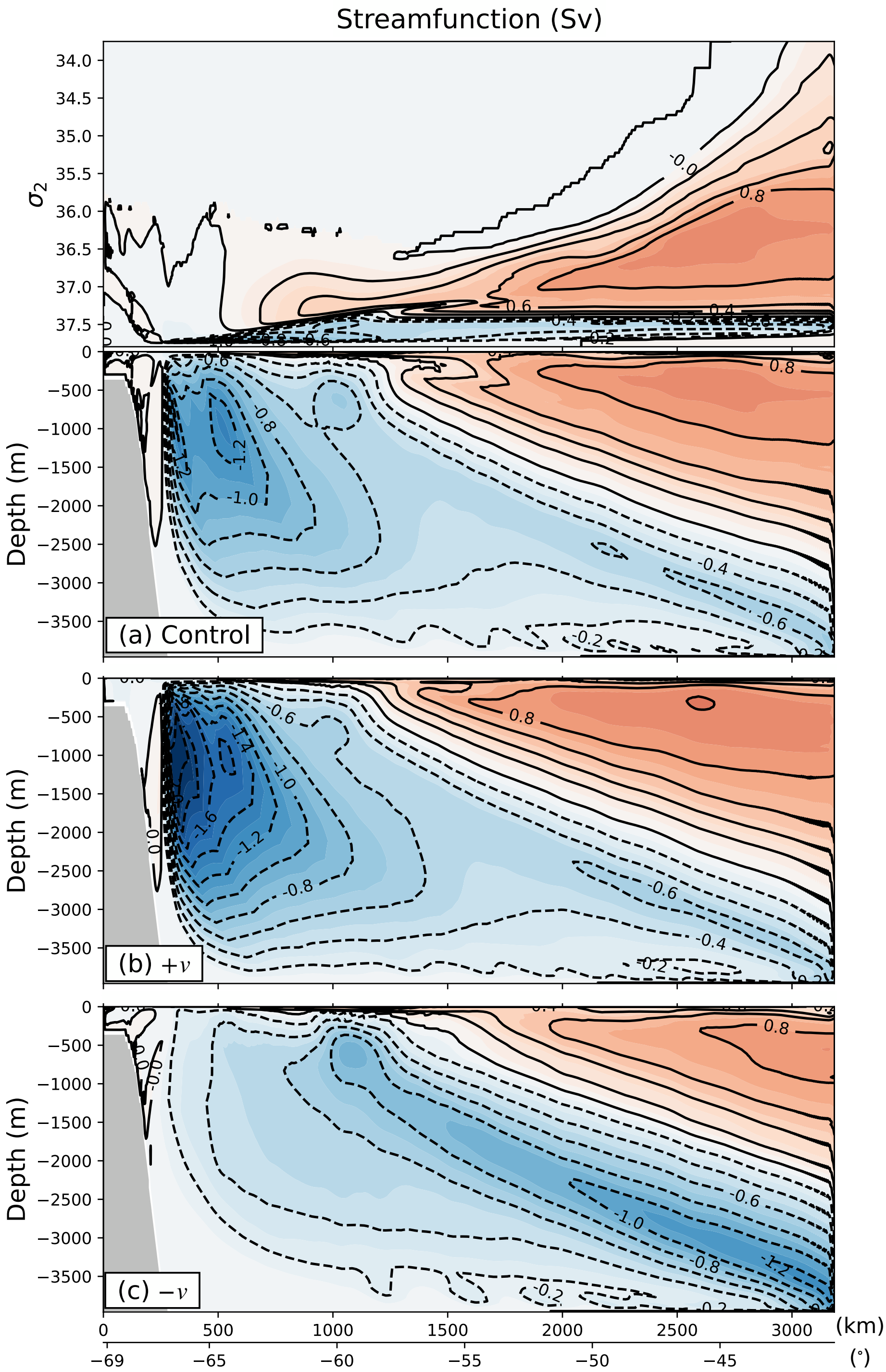

Figure 7. (a) Annually averaged residual streamfunction, Ψ, in σ_2 coordinate and depth coordinate in Control using both shading and contours. The annually averaged Ψ in (b) $+v$ and (c) $-v$ are shown only in depth coordinates. Ψ is in Sv ($= 10^6$ m^3 s^{-1}). The gray shading marks the topography.

Nishikawa et al., 2013; Al-Shehhi et al., 2021), which can be written as

$$A = F - \frac{\partial D}{\partial \sigma}, \tag{5}$$

where F is associated with surface fluxes, and the second term is associated with diffusive fluxes within the ocean. F, known as "transformation rate", can be written using the heat flux ($\mathcal{Q}_{net}$) and freshwater flux ($\mathcal{F}_{FW}$) so that

$$F \quad = \quad \frac{\partial}{\partial \sigma} \iint_{\mathcal{A}_s(\sigma,t)} \left(\frac{\alpha}{c_w} \mathcal{Q}_{net} + \rho_0 \beta S \mathcal{F}_{FW} \right) d\mathcal{A}. \tag{6}$$

Here, ρ_0 is the reference density, α is the thermal expansion coefficient for seawater, c_w is the heat capacity of water, β is the haline contraction coefficient and S is the local surface salinity. Both $\mathcal{Q}_{net}$ and $\mathcal{F}_{FW}$ are positive when they increase the surface density.

5.2.1 Contribution from surface heat flux

The surface heat flux leads to a positive water-mass transformation rate (increasing density) in fall and winter but a negative rate (decreasing density) in spring and summer (Fig. 8(c,f,i,l)). During fall and winter when the air temperature is colder than the surface ocean temperature, there is a oceanic heat loss that leads to an increase in surface density. This densification is particularly evident in the seasonal sea ice zone (37.5 $> \sigma_2 >$37.0 kg m^{-3}) and in the water-mass with $\sigma_2 >$ 37.5 kg m^{-3} located in the region to the south of 65°S, which suggests that there is considerable heat loss whenever there is an opening in the sea ice in fall and winter. By definition, the volume flux associated with a positive water-mass transformation rate is toward higher density class, which implies that the surface heat flux contributes to the poleward transport of the surface water in fall and winter. In fact, the lower cell extends equatorward during this season, supporting the surface poleward transport (not shown). As the season progresses, the ocean takes up the heat from the atmosphere, and the surface density decreases until the fall when the ocean starts to lose heat to the atmosphere again, which means that the heat flux acts to drive the equatorward transport of the surface water and feeds the upper cell. This is further supported by the poleward extension of the upper cell that has the equatorward transport near the surface during this season (not shown).

The southerly wind anomaly, $+v$, slightly reduces the positive water-mass transformation rate by the surface heat flux in winter, but amplifies the negative rate in summer (red lines in Fig. 8(a,g)). These changes are related to the sea ice extent. In $+v$,

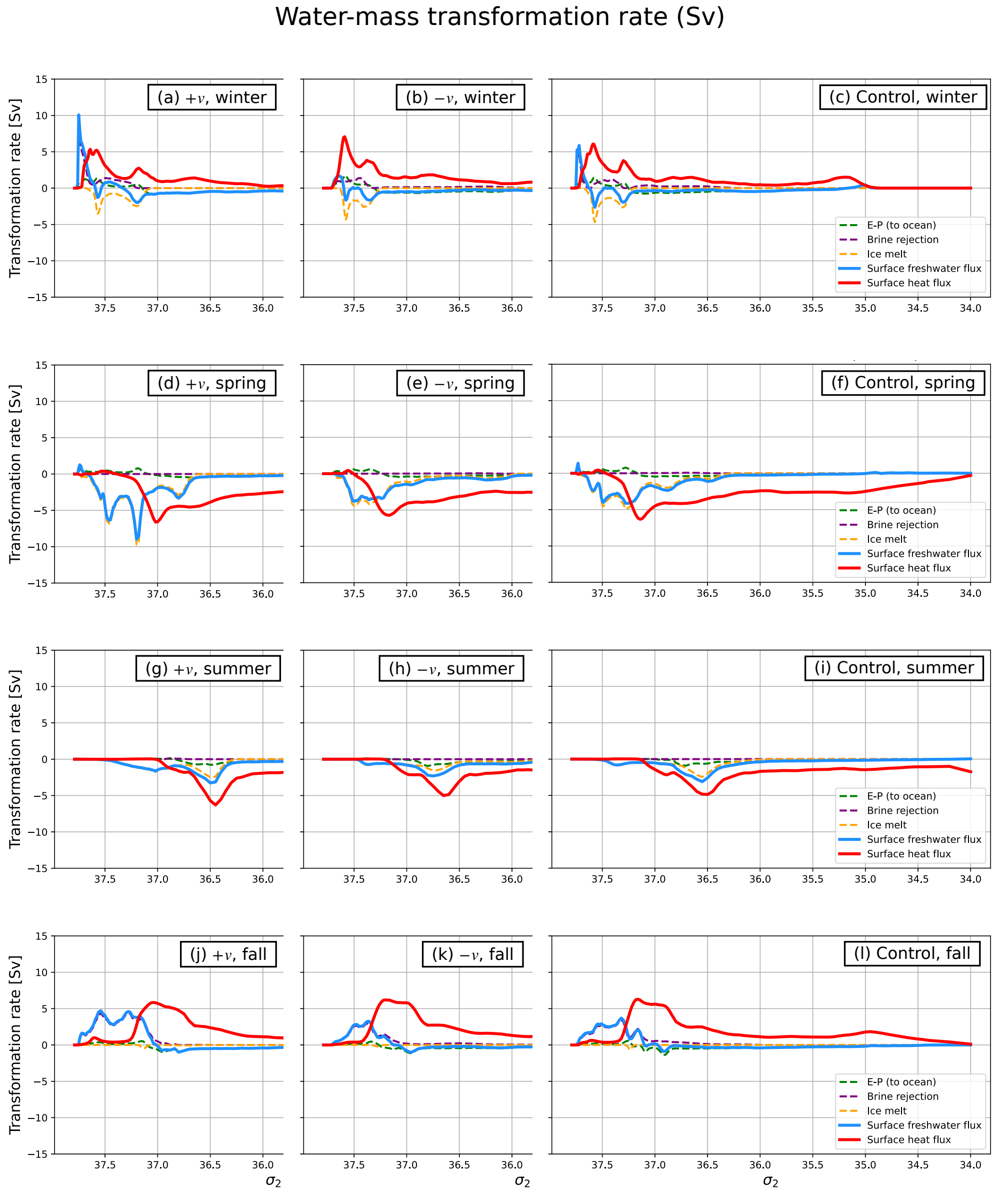

Figure 8. The water-mass transformation rate by surface heat flux (solid red) and freshwater flux (solid blue) in (a,d,g,j) $+v$, (b,e,h,k) $-v$, and (c,f,i,l) control run for austral (a-c) winter (July-September), (d-f) spring (October-December) (g-i) summer (January-March) and (j-k) fall (April-June). Positive values indicate an increase in the density of the sea water. The transformation rate by freshwater flux is partitioned into the difference between evaporation and precipitation (dashed green), and ocean-ice interaction that is the sum of brine rejection (dashed purple) and sea ice melting (dashed orange).

the larger sea ice extent in winter (Fig. 4(a)) limits the air-sea heat exchange more than in the control run, resulting in reduced heat loss. Leads and polynyas in Fig. 4(e) occur in the water-mass of $\sigma_2 \sim 37.7$ kg m^{-3} and serve as a site of heat loss and densification, as marked by the peak in the water-mass transformation rate in winter (Fig. 8(a)). In summer, however, $+v$ has a smaller sea ice extent than the control run, allowing more heat uptake and a greater negative transformation rate.

The northerly wind anomaly leads to a marginal increase in the positive transformation rate in winter when compared with CTRL (Fig. 8(b)). This increase occurs in the water-mass of $\sigma_2 \sim 37.6$ kg m^{-3} that can be found near 61°S in winter where the sea ice concentration in $-v$ is lower than CTRL. In summer, the size of negative water-mass transformation rate by the heat flux in $-v$ is comparable with CTRL, but there is a shift of the negative peak toward higher density class in $-v$ (Fig. 8(h)), which is associated with the higher density of the surface water. The lower sea ice seasonal variability in $-v$ results in the reduced equatorward freshwater transport, leading to a higher surface density than the other simulations.

5.2.2 Contribution from surface freshwater flux

The freshwater flux can be partitioned by two components in this channel model: freshwater flux between atmosphere and ocean, and between sea ice and ocean. The freshwater flux between atmosphere and ocean results from the difference between evaporation and precipitation, while sea ice formation and melting determine the freshwater flux between sea ice and ocean. The size of the water-mass transformation rate by freshwater flux is generally smaller than that by heat flux in the control simulation, except where sea ice formation and melting occur (Fig. 8(c,f,i,l)). In winter, the sea ice production has a positive transformation rate in the highest density class, showing that it is directly involved with bottom water formation (dashed purple line in Fig. 8(c)). The water-mass that becomes the bottom water is cooled by surface heat fluxes at $\approx \sigma_2 = 37.6$. The final increase in density is supplied through brine rejection from sea ice formation. In spring and summer, the freshening of the surface water by sea ice melting occurs in a lower density class than that of sea ice formation, indicating that there is a net freshwater transport from dense water-masses to lighter water-masses (dashed orange lines in Fig. 8(f,i)). The transformation rate by the freshwater flux between the atmosphere and the ocean shows a negligible contribution in the region south of the seasonal sea ice zone with 37.2 kg m^{-3} > σ_2 (dashed green lines in Fig. 8(c,f,i,l)), which can be explained by the presence of the sea ice that blocks the freshwater flux between them.

The southerly wind anomaly amplifies the water-mass transformation rate by freshwater flux (Fig. 8(a,d,g,j)). In particular, the sea ice formation and melting contribute to this amplification, showing nearly 10 Sv in winter and -10 Sv in spring, respectively. The increased positive transformation rate in winter is consistent with the intensification of the deep convection and the lower cell in $+v$ (Fig. 7(b)). The enhanced lower cell leads to a systematic warming along the upwelling branch (Fig. 6(a,b)), which contributes to the sea surface warming and sea ice retreat in $+v$ in summer when the surface temperature warming is nearly 1°C. In spring, the enhanced negative transformation rate in the seasonal sea ice zone suggests the largest freshwater flux into the ocean by the sea ice melting among the three simulations, which is in agreement with the lowest sea ice extent in $+v$ (Fig. 4(a)). This freshwater flux into the ocean leads to the lower surface salinity (Fig. 6(a,b)). Considering the transformation rates by both heat and freshwater flux, the volume transport toward lower density class in spring is the greatest in $+v$, leading to a slight increase of the upper cell (Fig. 7(b)).

In contrast, the deep convection is nearly absent in $-v$, and the sea ice formation and melting tend to occur only in the seasonal sea ice zone (Fig. 8(b,e,h,k)). As a result, the lower cell loses its strength by nearly 50% compared with the control simulation (Fig. 7(c)). The weakening of lower cell reduces the upwelling of relatively warm water, leading to the decrease of sea surface temperature (Fig. 6(c,d)). The upper cell also slightly loses the strength, and this is in agreement with the reduced negative transformation rate in the seasonal sea ice zone, and increased surface salinity (Fig. 6(c,d)). The reduced intensity of the formation rate by brine rejection and sea ice melting is consistent with a smaller seasonal cycle of sea ice, which is indeed observed in $-v$ (Fig. 4(a,b)).

6 Conclusion and Discussion

The surface wind near Antarctic sea ice plays a critical role in sea ice and oceanic processes that lead to bottom water formation and control the lower cell of the residual meridional overturning circulation. In this study, we aim to answer the question of how the strength of the meridional wind influences sea ice distribution and ocean circulation in the Southern Ocean using observations and an idealized eddy-resolving coupled ocean - sea ice model. The idealized configuration of the model allows us to eliminate complications due to zonal asymmetry and interannual variability while successfully reproducing not only the mean states of the sea ice and oceanic variables but also the two meridional overturning cells.

The sea ice and oceanic states and meridional circulation show distinct responses depending on the sign of the perturbation in the meridional wind near the sea ice zone. The southerly wind perturbation increases the seasonal variation in the sea ice extent: broader sea ice extent in austral winter but smaller in austral summer compared with the control simulation. The seasonal variation in the sea ice volume also becomes greater than the control simulation, indicating the enhancement of sea ice production and the equatorward freshwater transport. There is a substantial increase in leads and polynyas under the southerly wind perturbation in winter, where there is an oceanic heat loss and salt flux into the ocean due to sea ice formation. The water-mass transformation rate analysis reveals that these changes in the surface buoyancy flux result in volume fluxes towards higher density classes, eventually forming bottom water. The enhancement of bottom water formation strengthens the lower cell of the residual meridional overturning circulation and increases the rate at which relatively warm water is upwelled towards the summertime sea ice edge, promoting more sea ice melt there.

The northerly wind perturbation leads to the opposite response in the sea ice and ocean circulation. The seasonal variation of the sea ice extent is reduced with summertime extent increased and wintertime extent decreased. The sea ice volume, however, is larger in the $-v$ simulation than the other two simulations in all seasons, suggesting that the thickness of the sea ice is the greatest with the northerly meridional wind perturbation. This is especially true in winter when sea ice extent is the smallest, but volume is largest. The larger volume of sea ice in higher latitudes (south of 65°S) suppresses the surface buoyancy flux and the formation of bottom water, as shown by the water-mass transformation analysis. As a result, the lower cell and the upwelling of the relatively warm water weaken, contributing to greater sea ice extent and volume in the summer.

The simplicity of this study may not fully explain the observed and anticipated changes to sea ice and ocean circulation, especially if the wind forcing has zonally asymmetric components and interacts with orography. In addition, the time-invariant wind perturbations in our experiments are not consistent with the seasonal differences in the observed meridional wind trend (Hazel & Stewart, 2019). These shortcomings will be addressed in future studies where the meridional wind perturbations force a global ocean - sea ice model.

The results from this idealized model clearly show that meridional wind perturbations near the Antarctic sea ice region can have substantial and widespread impacts on the sea ice and ocean circulation. A series of well-coordinated processes between the sea ice and buoyancy-driven ocean circulation deliver the impact of surface wind perturbations down to the bottom of the Southern Ocean, emphasizing the importance of better representing the meridional winds for a more accurate simulation of the sea ice and the Southern Ocean. This is particularly important given that there is a relatively large spread in the surface wind among the existing reanalysis products (Dong et al., 2020). Hence, the results from this study may provide a guideline on what to anticipate in sea ice and Southern Ocean simulations when a particular reanalysis product is chosen to force the model.

The results from these simple experiments also show how to connect interannual and long-term sea ice variability to the meridional wind. As discussed in section 2, observed sea ice extent anomalies are correlated with meridional wind anomalies in both summer and winter. In addition, future projections of meridional wind near the Antarctic sea ice indicate we should anticipate wind driven changes to the sea ice and oceanic states in the Southern Ocean. CMIP6 models suggest an overall weakening of the southerly wind by 2% and 7% at the end of the century under the SSP2-4.5 and SSP5-8.5, respectively, but local changes in the meridional wind range between approximately -0.5 and 0.5 m s^{-1} (Neme et al., 2022). If the results from this study are linearly applied, then these meridional wind perturbations could result in a change of up to 25% in the strength of the lower cell locally. If these meridional wind changes align with dense shelf water formation regions, then we are likely to see significant changes to the formation of bottom water.

Data Availability Statement

The satellite sea-ice concentration data used in the study are available at NASA National Snow and Ice Data Center (`https://nsidc.org/data/NSIDC-0051/versions/2`). The ERA5 reanalysis data for 10-meter winds can be accessed from the Copernicus Climate Data Store (`https://cds.climate.copernicus.eu/cdsapp#!/dataset/reanalysis-era5-single-levels-monthly-means?tab=form`). Both datasets are freely available with citations DiGirolamo et al. (2022) and Hersbach et al. (2023) respectively. The MIT-gcm can be obtained from http://mitgcm.org website. The model's configuration and output are available upon request.

Acknowledgments

HS and YC acknowledge support from a National Research Foundation of Korea (NRF) grant funded by the Korean government (MSIT) (2022R1A2C1009792 and 2018R1A5A1024958). HS is also supported by the Research Program for the carbon cycle between oceans, land, and atmosphere of the NRF funded by the Ministry of Science and ICT(2022M3I6A108599012). EWD is the recipient of an Australian Research Council Discovery Project (DP230102994) funded by the Australian Government. This project received grant funding from the Australian Government as part of the Antarctic Science Collaboration Initiative program (ASCI000002). JM acknowledges support from the NASA PO program, award number: 80NSSC21K0557.H. Song acknowledges support from a National Research Foundation of Korea (NRF) grant funded by the Korean government (MSIT) (2022R1A2C1009792). EWD is the recipient of an Australian Research Council Discovery Project (DP230102994) funded by the Australian Government. This project received grant funding from the Australian Government as part of the Antarctic Science Collaboration Initiative program (ASCI000002). JM acknowledges support from the NASA PO program, award number: 80NSSC21K0557.

References

Abernathey, R. P., Cerovecki, I., Holland, P. R., Newsom, E., Mazloff, M., & Talley, L. D. (2016). Water-mass transformation by sea ice in the upper branch of the Southern Ocean overturning. *Nature Geoscience*, *9*, 596–601.

Adcroft, A., Hill, C., Campin, J.-M., Marshall, J., & Heimbach, P. (2004). Overview of the formulation and numerics of the MIT GCM. In *Proceedings of the*

ECMWF Seminar Series on Numerical Methods, Recent Developments in Numerical Methods for Atmosphere and Ocean Modelling (pp. 139–149). ECMWF.

Adcroft, A., Hill, C., & Marshall, J. (1997). Representation of topography by shaved cells in a height coordinate ocean model. *Monthly Weather Review*, *125*, 2293–2315.

Al-Shehhi, M. R., Song, H., Scott, J., & Marshall, J. (2021). Water mass transformation and overturning circulation in the arabian gulf. *Journal of Physical Oceanography*, *51*(11), 3513–3527. doi: 10.1175/JPO-D-20-0249.1

Armour, K. C., Marshall, J., Scott, J. R., Donohoe, A., & Newsom, E. R. (2016). Southern Ocean warming delayed by circumpolar upwelling and equatorward transport. *Nature Geoscience*, *9*, 549–554. doi: 10.1038/ngeo2731

Bader, J., Flügge, M., Kvamstø, N. G., Mesquita, M. D., & Voigt, A. (2013). Atmospheric winter response to a projected future antarctic sea-ice reduction: A dynamical analysis. *Climate Dynamics*, *40*, 2707–2718.

Barthélemy, A., Goosse, H., Mathiot, P., & Fichefet, T. (2012). Inclusion of a katabatic wind correction in a coarse-resolution global coupled climate model. *Ocean Modelling*, *48*, 45–54.

Bintanja, R., van Oldenborgh, G. J., Drijfhout, S., Wouters, B., & Katsman, C. (2013). Important role for ocean warming and increased ice-shelf melt in antarctic sea-ice expansion. *Nature Geoscience*, *6*(5), 376–379.

Bracegirdle, T. J., & Marshall, G. J. (2012). The reliability of antarctic tropospheric pressure and temperature in the latest global reanalyses. *Journal of Climate*, *25*(20), 7138–7146.

Campbell, E. C., Wilson, E. A., Moore, G. W. K., Riser, S. C., Brayton, C. E., Mazloff, M. R., & Talley, L. D. (2019). Antarctic offshore polynyas linked to Southern Hemisphere climate anomalies. *Nature*, *570*(7761), 319–325. doi: 10.1038/s41586-019-1294-0

Cavalieri, D. J., & Parkinson, C. L. (2008). Antarctic sea ice variability and trends, 1979–2006. *Journal of Geophysical Research: Oceans*, *113*(C7).

Comiso, J. C., & Nishio, F. (2008). Trends in the sea ice cover using enhanced and compatible amsr-e, ssm/i, and smmr data. *Journal of Geophysical Research: Oceans*, *113*(C2).

DiGirolamo, N., Parkinson, C. L., Cavalieri, D. J., Gloersen, P., & Zwally., H. J. (2022). *Sea ice concentrations from nimbus-7 smmr and dmsp ssm/i-ssmis passive microwave data, version 2* [dataset]. NASA National Snow and Ice Data Center Distributed Active Archive Center. Retrieved from `https://nsidc.org/data/NSIDC-0051/versions/2` doi: 10.5067/MPYG15WAA4WX

Doddridge, E. W., Marshall, J., Song, H., Campin, J.-M., & Kelley, M. (2021). Southern ocean heat storage, reemergence, and winter sea ice decline induced by summertime winds. *Journal of Climate*, *34*(4), 1403–1415.

Dong, X., Wang, Y., Hou, S., Ding, M., Yin, B., & Zhang, Y. (2020). Robustness of the recent global atmospheric reanalyses for Antarctic near-surface wind speed climatology. *Journal of Climate*(10), 4027–4043. doi: 10.1175/JCLI-D-19-0648.1

Ferrari, R., Jansen, M. F., Adkins, J. F., Burke, A., Stewart, A. L., & Thompson, A. F. (2014). Antarctic sea ice control on ocean circulation in present and glacial climates. *Proceedings of the National Academy of Sciences*, *111*(24), 8753-8758. doi: 10.1073/pnas.1323922111

Ferreira, D., Marshall, J., Bitz, C. M., Solomon, S., & Plumb, A. (2015). Antarctic ocean and sea ice response to ozone depletion: A two-time-scale problem. *Journal of Climate*, *28*(3), 1206–1226. doi: 10.1175/JCLI-D-14-00313.1

Gaspar, P., Grégoris, Y., & Lefevre, J.-M. (1990). A simple eddy kinetic energy model for simulations of the oceanic vertical mixing: Tests at station Papa and Long-Term Upper Ocean Study site. *Journal of Geophysical Research: Oceans*, *95*(C9), 16179–16193.

Harangozo, S. A. (2006). Atmospheric circulation impacts on winter maximum sea ice extent in the west Antarctic Peninsula region (19792001). *Geophysical Research Letters*, *33*(2). doi: 10.1029/2005GL024978

Haumann, F. A., Notz, D., & Schmidt, H. (2014). Anthropogenic influence on recent circulation-driven antarctic sea ice changes. *Geophysical Research Letters*, *41*(23), 8429–8437.

Hazel, J. E., & Stewart, A. L. (2019). Are the near-Antarctic easterly winds weakening in response to enhancement of the southern annular mode? *Journal of Climate*, *32*(6), 1895–1918. doi: 10.1175/JCLI-D-18-0402.1

Hersbach, H., Bell, B., Berrisford, P., Biavati, G., Hornyi, A., Sabater, J. M., . . . Thpaut, J.-N. (2023). *Era5 monthly averaged data on single levels from 1940 to present* [dataset]. Copernicus Climate Change Service (C3S) Climate Data Store (CDS). Retrieved from `https://cds.climate.copernicus.eu/cdsapp#!/dataset/reanalysis-era5-single-levels-monthly-means?tab=form` (Accessed on 10-MAR-2021) doi: 10.24381/cds.f17050d7

Hobbs, W. R., Klekociuk, A. R., & Pan, Y. (2020). Validation of reanalysis southern ocean atmosphere trends using sea ice data. *Atmospheric Chemistry and Physics*, *20*(23), 14757–14768.

Holland, P. R., & Kwok, R. (2012). Wind-driven trends in Antarctic sea-ice drift. *Nat. Geosci.*, *5*, 872–875.

Huai, B., Wang, Y., Ding, M., Zhang, J., & Dong, X. (2019). An assessment of recent global atmospheric reanalyses for antarctic near surface air temperature. *Atmospheric Research*, *226*, 181–191.

Kidston, J., Taschetto, A. S., Thompson, D. W. J., & England, M. H. (2011). The influence of southern hemisphere sea-ice extent on the latitude of the mid-latitude jet stream. *Geophysical Research Letters*, *38*(15). doi: 10.1029/2011GL048056

Kim, S., & Stössel, A. (1998). On the representation of the Southern Ocean water masses in an ocean climate model. *J. Geophys. Res.*, *103*(C11), 24891–24906.

Kwok, R., Pang, S. S., & Kacimi, S. (2017). Sea ice drift in the Southern Ocean: Regional patterns, variability, and trends. *Elementa: Science of the Anthropocene*, *5*, 32. doi: 10.1525/elementa.226

Large, W. G., & Pond, S. (1982). Sensible and latent head flux measurements over the ocean. *J. Phys. Oceanogr.*, *12*, 464–482.

Large, W. G., & Yeager, S. G. (2009). The global climatology of an interannually varying air-sea flux data set. *Climate Dyn.*, *33*, 341–364. doi: 10.1007/s00382-008-0441-3

Libera, S., Hobbs, W., Klocker, A., Meyer, A., & Matear, R. (2022). Ocean-sea ice processes and their role in multi-month predictability of antarctic sea ice. *Geophysical Research Letters*, *49*(8), e2021GL097047. Retrieved from `https://agupubs.onlinelibrary.wiley.com/doi/abs/10.1029/2021GL097047` (e2021GL097047 2021GL097047) doi: https://doi.org/10.1029/2021GL097047

Locarnini, R. A., Mishonov, A. V., Antonov, J. I., Boyer, T. P., Garcia, H. E., Baranova, O. K., … Seidov, D. (2013). Temperature. In S. Levitus (Ed.), *World ocean atlas 2013* (Vol. 1, p. 40). NOAA Atlas NESDIS.

Marshall, J., Adcroft, A., Hill, C., Perelman, L., & Heisey, C. (1997). A finite-volume, incompressible Navier Stokes model for studies of the ocean on parallel computers. *J. Geophysical Res.*, *102*(C3), 5753–5766.

Marshall, J., Hill, C., Perelman, L., & Adcroft, A. (1997). Hydrostatic, quasi-hydrostatic, and nonhydrostatic ocean modeling. *J. Geophysical Res.*, *102*(C3), 5733–5752.

Marshall, J., Jamous, D., & Nilsson, J. (1999). Reconciling thermodynamic and dynamic methods of computation of water-mass transformation rates. *Deep-Sea Res. I*, *46*(4), 545–572.

Marshall, J., Jones, H., & Hill, C. (1998). Efficient ocean modeling using non-hydrostatic algorithms. *J. Mar. Syst.*, *18*, 115–134.

Marshall, J., & Speer, K. (2012). Closure of the meridional overturning circulation through Southern Ocean upwelling. *Nature Geoscience*, *5*(3), 171–180. doi: 10.1038/ngeo1391

Neme, J., England, M. H., & McC. Hogg, A. (2022). Projected changes of surface winds over the Antarctic continental margin. *Geophysical Research Letters*, *49*(16), e2022GL098820. doi: 10.1029/2022GL098820

Nishikawa, S., Tsujino, H., Sakamoto, K., & Nakano, H. (2013). Diagnosis of water mass transformation and formation rates in a high-resolution GCM of the North Pacific. *Journal of Geophysical Research: Oceans*, *118*(3), 1051–1069. doi: 10.1029/2012JC008116

Parish, T. R., & Waight III, K. T. (1987). The forcing of antarctic katabatic winds. *Monthly Weather Review*, *115*(10), 2214–2226.

Parkinson, C. L., & Cavalieri, D. J. (2012). Antarctic sea ice variability and trends, 1979–2010. *The Cryosphere*, *6*(4), 871–880.

Pauling, A. G., Bitz, C. M., Smith, I. J., & Langhorne, P. J. (2016). The response of the southern ocean and antarctic sea ice to freshwater from ice shelves in an earth system model. *Journal of Climate*, *29*(5), 1655–1672.

Pavelsky, T. M., Boé, J., Hall, A., & Fetzer, E. J. (2011). Atmospheric inversion strength over polar oceans in winter regulated by sea ice. *Climate dynamics*, *36*, 945–955.

Pinardi, N., Cessi, P., Borile, F., & Wolfe, C. L. P. (2019). The mediterranean sea overturning circulation. *Journal of Physical Oceanography*, *49*(7), 1699 - 1721. doi: 10.1175/JPO-D-18-0254.1

Purich, A., Cai, W., England, M. H., & Cowan, T. (2016). Evidence for link between modelled trends in antarctic sea ice and underestimated westerly wind changes. *Nature communications*, *7*(1), 10409.

Rye, C. D., Marshall, J., Kelley, M., Russell, G., Nazarenko, L. S., Kostov, Y., ... Hansen, J. (2020). Antarctic glacial melt as a driver of recent Southern Ocean climate trends. *Geophysical Research Letters*, *47*(11), e2019GL086892.

Schroeter, S., & Sandery, P. A. (2022). Large-ensemble analysis of Antarctic sea ice model sensitivity to parameter uncertainty. *Ocean Modelling*, *177*, 102090.

Smith, D. M., Dunstone, N. J., Scaife, A. A., Fiedler, E. K., Copsey, D., & Hardiman, S. C. (2017). Atmospheric response to Arctic and Antarctic sea ice: The importance of oceanatmosphere coupling and the background state. *Journal of Climate*, *30*(12), 4547 - 4565. doi: 10.1175/JCLI-D-16-0564.1

Stammerjohn, S. E., Drinkwater, M. R., Smith, R. C., & Liu, X. (2003). Ice-atmosphere interactions during sea-ice advance and retreat in the western antarctic peninsula region. *Journal of Geophysical Research: Oceans*, *108*(C10). doi: 10.1029/2002JC001543

Stein, K., Timmermann, A., Kwon, E. Y., & Friedrich, T. (2020). Timing and magnitude of southern ocean sea ice/carbon cycle feedbacks. *Proceedings of the National Academy of Sciences*, *117*(9), 4498-4504. doi: 10.1073/pnas.1908670117

Tamura, T., Ohshima, K. I., & Nihashi, S. (2008a). Mapping of sea ice production for antarctic coastal polynyas. *Geophysical Research Letters*, *35*(7). doi: 10.1029/2007GL032903

Tamura, T., Ohshima, K. I., & Nihashi, S. (2008b). Mapping of sea ice production for Antarctic coastal polynyas. *Geophys. Res. Lett.*, *35*, L07606. doi: 10.1029/2007GL032903

Thompson, D. W., & Solomon, S. (2002). Interpretation of recent southern hemisphere climate change. *Science*, *296*(5569), 895–899.

Turner, J., Comiso, J. C., Marshall, G. J., Lachlan-Cope, T. A., Bracegirdle, T., Maksym, T., . . . Orr, A. (2009). Non-annular atmospheric circulation change induced by stratospheric ozone depletion and its role in the recent increase of antarctic sea ice extent. *Geophysical Research Letters*, *36*(8). doi: 10.1029/2009GL037524

Turner, J., Hosking, J. S., Marshall, G. J., Phillips, T., & Bracegirdle, T. J. (2016). Antarctic sea ice increase consistent with intrinsic variability of the Amundsen Sea Low. *Climate Dynamics*, *46*, 2391–2402.

Wagner, T. J. W., Eisenman, I., & Mason, H. C. (2021). How sea ice drift influences sea ice area and volume. *Geophysical Research Letters*, *48*(19), e2021GL093069. Retrieved from `https://agupubs.onlinelibrary.wiley.com/doi/abs/10.1029/2021GL093069` (e2021GL093069 2021GL093069) doi: https://doi.org/10.1029/2021GL093069

Walin, G. (1982). On the relation between sea-surface heat flow and thermal circulation in the ocean. *Tellus*, *34*, 187–195. doi: 10.1111/j.2153-3490.1982.tb01806.x

Wall, C. J., Kohyama, T., & Hartmann, D. L. (2017). Low-cloud, boundary layer, and sea ice interactions over the southern ocean during winter. *Journal of Climate*, *30*(13), 4857–4871.

Zweng, M., Reagan, J., Antonov, J., Locarnini, R., Mishonov, A., Boyer, T., . . . Biddle, M. (2013). Salinity. In S. Levitus (Ed.), *World ocean atlas 2013* (Vol. 2, p. 39). NOAA Atlas NESDIS.